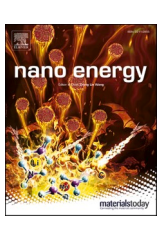


Contents lists available at ScienceDirect

Nano Energy

journal homepage: www.elsevier.com/locate/nanoen





Construction of efficient silicon solar cells through polymetallic oxidation-reduction triggered by thermite reaction

Yongsheng Li ^{a,1}, Ziwei Chen ^{a,1}, Bo Zhang ^a, Haibiao Chen ^b, Rui Zhou ^a, Boweng Nan ^a, Wenguang Zhao ^a, Ke Li ^a, Bolin Zhao ^a, Yinguo Xiao ^a, Jian Liu ^{a,*}, Jun Chen ^{c,*}, Yuan Lin ^{d,*}, Feng Pan ^{a,*}

- ^a School of Advanced Materials, Peking University, Shenzhen Graduate School, Shenzhen 518055, China
- ^b Institute of Marine Biomedicine, Shenzhen Polytechnic, Shenzhen 518055, China
- ^c Institute of Zhejiang University-Quzhou, Quzhou 324000, China
- d Key Laboratory of Photochemistry, Institute of Chemistry, Chinese Academy of Sciences, Beijing 100190, China

ARTICLEINFO

Keywords: Thermite reaction Oxidation-reduction Glass frits Sb/Mo co-doped Al-Si interface Solar cells

ABSTRACT

Optimal metal-semiconductor contact interface is crucial for semiconductor devices, particularly for silicon solar cells aluminum-silicon contact is a key to improve the efficiency of the cell. In this work, a new type of Sb_2O_3 - MoO_3 - B_2O_3 glass frits that can trigger a thermite reaction was utilized to improve the Al-Si interface. The low melting temperatures of these glass frits enhance the effect of thermite reaction by providing solid-liquid contact, which enables gradient distribution of the elements and leads to differences in the valence states of the Al-Si layer at the inner and surface regions. The valence states of Al and Sb at the inner layer are higher than those at the surface, while Mo is the opposite. Metallic Mo with a matched work function can lower the potential barrier, thereby improving hole selectivity and enhancing the potential skip-step. As a result, the fabricated solar cell achieved a high open-circuit voltage, a high short-circuit current, and a low series resistance. Consequently, a power conversion efficiency of 19.94% was obtained for a monocrystalline silicon solar cell with full Al-BSF. This work not only presents a new hole-selective contact for silicon solar cells, but also introduces a new approach for regulating the distribution and valence states of interface elements for enhanced efficiency.

1. Introduction

Developing sustainable, affordable and clean energy is an important strategy to address the challenges of fossil energy depletion and environmental pollution in recent years. Among the various renewable energy sources, solar energy has gained significant attention and research focus worldwide due to its potential to provide clean power [1]. Crystalline silicon (c-Si) solar cells, being one of the mainstream photovoltaic technologies, have rapidly evolved as a competitive alternative to traditional fossil energy over the past decades. Research efforts in the field of c-Si solar cells have primarily aimed at improving their efficiency to ensure economical energy production [2,3]. One of the major challenges in c-Si solar cells is the recombination of photogenerated carriers at the metal silicon interface, which reduces the overall efficiency. Additionally, the high resistance of carrier collection poses a significant

barrier to efficient carrier extraction [4]. These limitations particularly impact P-type c-Si solar cells, which have the largest production capacity. Therefore, improving the efficiency of P-type c-Si solar cells is of paramount importance in current research endeavors.

In order to reduce the recombination of carriers at the metal silicon interface in p-Type c-Si solar cells, aluminum paste can be coated on the back surface of the cells to create a back surface field (BSF) layer and an aluminum-silicon (Al-Si) alloy layer through a high-temperature sintering process. In addition, it is important to implement a good Al-Si contact to mitigate the negative effect of high resistance and further increase the efficiency of the cells [5–7]. Al paste typically consists of glass frits, aluminum powder and an organic phase. As an inorganic functional material, glass frits play a key role in improving the performance of Al paste [8,9]. Glass frits are typically composed of boron oxide (B₂O₃) and other oxides, with Pb-Si-based and Zn-Bi-based glass

E-mail addresses: liujian@pkusz.edu.cn (J. Liu), qiujinchen@zju.edu.cn (J. Chen), linyuan@iccas.ac.cn (Y. Lin), panfeng@pkusz.edu.cn (F. Pan).

^{*} Corresponding authors.

¹ Y. L. and Z. C. contributed equally to this work

frits being commonly used in Al paste [10]. Jang et al. discovered that Pb-Si-based glass frits promoted the sintering of Al paste [8]. Bit-Na et al. found that increasing the proportion of low melting point oxide in glass frits reduced the glass transition temperature (T_p) , leading to better sintering and a thicker BSF layer [9]. Amick et al. also noted that a thicker BSF layer would increase the open-circuit voltage (V_{oc}) and the addition of an Al-Si contact would improve the efficiency of c-Si solar cells [11]. However, it is worth mentioning that lead-containing materials are not environmentally friendly, and the T_g of Zn-Bi-based glass frits is higher than 350 °C, which is not conducive to sintering. Furthermore, the melted glass frits and other powders may spread and form a layer on the back of the cells, which can also affect the photoelectric parameter of c-Si solar cells [12]. Some metal oxide films with hole selective contacts, such as molybdenum oxide (MoOx), aluminum oxide (Al₂O₃), titanium oxide (TiO₂), tungsten oxide (WO_x), antimony trioxide (Sb₂O₃)etc., have been used to reduce carrier recombination in not only c-Si solar cells but also other types of solar cells. However, the deposition of these films usually requires high-vacuum equipment [13-19]. Although the design of high-performance glass frits still has room for improvement, it remains a crucial yet relatively simple and effective way to improve Al paste and promote the efficiency of c-Si solar

Inspired by previous researches, a new type of glass frits for Al paste was designed using environmentally friendly elements and B2O3, Sb2O3 and MoO3 were selected, aligning with the concept of green development. The low melting points of Sb₂O₃ and MoO₃ were beneficial in lowering the T_g of glass frits, facilitating the formation of a solid-liquid interface between particles and consequently the thermite reaction. Moreover, metallic Mo generated in thermite reactions is known for its high work function could potentially improve the Al-Si contact [20,21]. Additionally, oxides with high work function have been reported to enhance the Al-Si interface, leading to improved passivation effect and hole selectivity [17,18,22-26]. In this work, a novel type of glass frits capable of triggering thermite reactions was developed to construct a Sb/Mo co-doped Al-Si interface. Compared to traditional Pb-Si-based glass frits, this new glass frits was found to promote cells efficiency from 19.31% to 19.94%. Subsequently, multiple detection methods were employed to investigate the Sb/Mo co-doped Al-Si interface and the reasons behind the observed efficiency improvement.

2. Experimental section

2.1. Materials synthesis

The recipe for the traditional Pb-Si-based glass frits (marked as Pb-g), used as control group, consisted of 67% PbO, 17% B_2O_3 , 10% SiO₂, and 6% ZnO, all measured in mass percentages. In brief, the fabrication process for Pb-g involved mixing the oxides powders in an alumina crucible and heating them at 1000 °C for half an hour in an air atmosphere, followed by water quenching to obtain Pb-g block. Pb-g powder was obtained by grinding the Pb-g block with ethanol in an agate mortar. Finally, the Pb-g powder was dried in a blast oven. The recipe for the B_2O_3 -Sb₂O₃-MoO₃ glass frits (marked as SM-g) consisted of 50.5% Sb₂O₃, 41.5% MoO₃, and 8% B_2O_3 . The fabrication process for SM-g was the same as that of Pb-g.

The blank Al paste without glass frits was prepared by mixing 70% Al powder (consisting of 25% of 2–3 μm and 45% of 5–6 μm), 5% Al-Si alloy powder, 24.5% organic carrier (consisting of ethyl cellulose N7, N200, acrylic resin, butyl carbitol acetate, hydrogenated castor oil, terpinol and alcohol ester dodecyl), and 0.5% dispersant (BYK-110, Germany). Pb-g was added to blank Al paste to prepare Pb-based Al paste (marked as P-Pb), and SM-g was added to blank Al paste to prepare SM-based Al paste (marked as P-SM).

The front silver paste used in this work is commercial silver paste (purchased from SAMSUNG SDI CO.,LTD.). The front electrode pattern was shown in Fig. S1.

By screen printing and co-firing in a belt furnace, Al-Si (made by Al paste) and Ag-Si contacts were formed on the monocrystalline silicon wafer (157 mm \times 157 mm, purchased from Wuxi Bokun Photovoltaic Technology Co., Ltd., China). The c-Si solar cells were fabricated using P-Pb and the P-SM following similar procedures and were marked as Cell-Pb and Cell-SM, respectively.

2.2. Materials characterizations

The crystalline structures of the samples were analyzed by X-ray diffraction (XRD) measurements with a Bruker D8 Discover diffractometer (Cu K α radiation with $\lambda=1.5405(6)$ Å within the 2θ range of $10-80^\circ$). The morphology and elemental distribution of the materials were further examined by scanning electron microscope (SEM, ZEISS SUPRA-55), transmission electron microscope (TEM, JEM–3200FS, 300 keV) and energy dispersive spectroscopy (EDS, OXFORD, X-MaxN TSR and X-max 80). X-ray photoelectron spectroscopy (XPS) tests were conducted using a Thermo Fisher ESCALAB 250X with a monochromatic Al K X-ray source to study the valence states of Al, Si, Sb and Mo. Thermal analyses were conducted on a TG/DTA analyzer (WCT-122, Beijing Hongyuan Co., Ltd., China) to determine the T_g of the glass frits and the sintering properties of Al paste.

2.3. Device performance measurements

The electrical parameters of the cells were measured using a pulsed solar simulator (PSL SCD, BERGER Lichttechnik GmbH & Co.KG). The contact resistance of Ag-Si and Al-Si, as well as the thin layer resistance of Al layer, were measured using a four-probe resistivity tester (KDY-1, Guangzhou Kunde Technology Co., Ltd., China), in 1.0 mA and ρ mode. The external quantum efficiency (EQE) and spectral response (SQ) curves of the cells were measured using a QE tester system (SCS1011, Zolix Instruments Co., Ltd., China). The surface potential of the Al-Si interfaces was measured using an atomic force microscope (AFM, Dimension Icon, Bruker Co., Germany) with Kelvin probe force microscopy (KPFM) using Pt/Ir-coated conducting tips (SCM-Pit) at a scan rate of 0.498 Hz. The samples of cells for the KPFM measurement were cut into 10 mm \times 5 mm pieces using a laser, and then polished by an Ar $^+$ ion beam milling technique (Leica EM TIC 3X, Leica Microsystems GmbH, Germany).

3. Result and discussion

Monocrystalline c-Si solar cells were fabricated using the Al-BSF cells manufacturing process. Fig. 1a illustrates the glass frits powder, Al paste, and cells fabrication process. For P-Pb (Pb containing paste), 1.5% of Pb-g (Pb-Si-based glass frits, the optimal addition amount) was added to the blank Al paste, while for P-SM (Sb-Mo containing paste), 0.75% of SM-g (B₂O₃-Sb₂O₃-MoO₃ glass frits, the optimal addition amount) was added to the blank Al paste, as listed in Tables S1 and S2 (Supporting Information). The monocrystalline c-Si solar cells were fabricated by using the P-Pb and the P-SM following similar procedures and were marked as Cell-Pb and Cell-SM, respectively. The monocrystalline c-Si solar cell was produced in standard industrial size (157 mm \times 157 mm) as shown in real device photograph in Fig. 1b, with silver fingers on the front and aluminum back field on the back. The XRD pattern of the SM-g shown in Fig. 1c displays broad peaks at around 27° and 51°, indicating a vitreous material [8]. The glass phase of the SM-g was formed by melting in the muffle furnace and quenching in water. The SM-g contained irregular blocky solid particles with a length and width of several microns (shown in Fig. S2, Supporting Information). DTA curve of the SM-g shown in Fig. 1d revealed a T_g of 279.7 °C, which is lower than that of Pb-g and comparable glass frits reported previously [8,9]. Previous research has proven that using glass frits with a lower T_g can enhance the sintering of Al particles [9], as the solid-liquid interface formed by glass melting at a low temperature allows for effective contact between glass

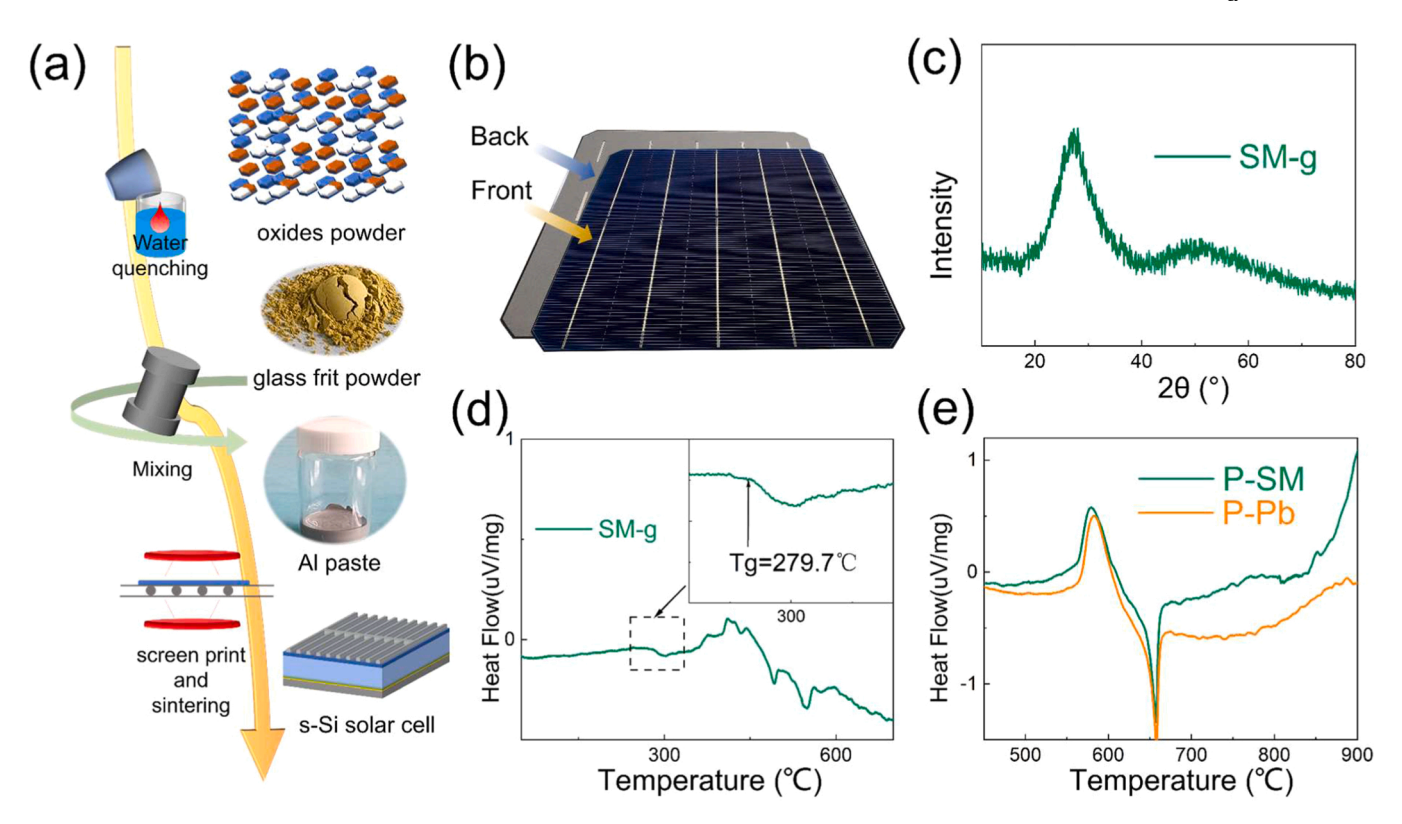


Fig. 1. Manufacturing process and characterization of glass frits and Al paste. (a) Schematic of the monocrystalline c-Si solar cell fabrication process. Top to bottom: oxides powder to glass frits powder via roasting and quenching, glass frits powder to Al paste via mixing, manufacturing c-Si solar cell by screen print and sintering; (b) Actual photo of monocrystalline c-Si cells in this work; (c) Crystal structure characterization on powder samples of the SM-g; (d-e) DTA curves of the SM-g, the Cell-SM and the Cell-Pb in air (heating rate of 10 °C/min).

frits and aluminum particles, providing favorable conditions for the thermite reaction. The DTA curve of P-SM Fig. 1e exhibits a steep sloping line from 670 °C to 900 °C with an obvious exothermic peak at about 900 °C, which is starting from approximately 690 °C. In contrast, the DTA curve of P-Pb shows a gentle sloping line without any obvious exothermic peak. The c-Si solar cells were produced by rapid sintering in an infrared mesh belt furnace. As the cells were in the peak temperature zone for only a few seconds, heating from the thermite reaction plays a critical role by promoting the metallization of the back surface to improve the efficiency of devices [27].

The photovoltaic performance parameters of Cell-SM, Cell-Pb, and a commercial cell from previous research are listed in Table 1. The measurements were conducted using a Berger Lichttechnik Pulsed solar simulator PSS-10 under the standard test condition of AM 1.5 G illumination, 1000 W/m², and 25 °C. Cell-SM demonstrated impressive performance, with a V_{oc} of 645.3 mV, a short-circuit current (I_{sc}) of 9.519 A and a series resistance (R_s) of 2.472 m Ω . Notably, Cell-SM achieved a high fill factor (FF) of 79.6% and an impressive power conversion efficiency (PCE) of 19.94%, outperforming Cell-Pb (IV curves are shown in Fig. S3, Supporting Information).

A radar chart in Fig. 2a is used to directly compare the performance parameters of Cell-SM and Cell-Pb. It is evident that Cell-SM

Table 1Photovoltaic (PV) performance parameters of the Cell-SM, the Cell-Pb in this work and Cell-com* (commercial cell in other work).

Cell	Voc (mV)	Isc (A)	Jsc (mA/cm^-2)	Rs (mΩ)	FF (%)	η (%)
Cell-SM	645.3	9.519	38.99	2.472	79.6	19.94
Cell-Pb	639.7	9.406	38.53	3.257	78.4	19.31
Cell-com ^a	641.2	/	38.46	/	80.33	19.81

^a commercial cell in other work [28].

outperformed Cell-Pb in multiple aspects, with lower Rs and higher values for V_{oc} , I_{sc} , FF, and PCE. The improvement in V_{oc} is likely attributed to an optimized BSF, while the increase in I_{SC} and decrease in Rs are probably due to an optimized of Al-Si contact. These improvements may be achieved through the thermite reaction and its side reactions. Fig. 2c-e present scatter diagrams and histograms comparing J_{sc} , V_{oc} , PCE, FF, and R_S of cells in this work and same type of cells (p-type monocrystalline silicon solar cell with a full-area Al-BSF) in previous works [28-34]. Compared to commercial cell of the same type in literature, Cell-SM exhibited competitive performance parameters [28]. Further photoelectronic characterization in Fig. 2b, including external quantum efficiency (EQE) and spectral response (SR) spectra (the equivalent current in the long wavelength range of 850-1100 nm, shown in Fig. S4), indicates that the back surface structure of Cell-SM was effectively optimized, leading to reduced carrier recombination and improved carrier collection at the back surface in the long wavelength range (850-1100 nm) [35]. This reduction in back surface recombination has a significant impact on V_{oc} and J_{sc} , while the effective carrier collection indicates improved Al-Si contact and reduced R_s , possibly attributed to the optimization of the Al-Si interface.

To further characterize the optimization of the back surface structure, the surface potential of the Al-Si interface was analyzed using Kelvin probe force microscopy (KPFM). Fig. 3a, b show the in-situ surface potential maps obtained during the scan, where brighter regions with higher surface potential on the right represent Al and darker regions with lower potential on the left represent Si. The morphology images of the same cross-section are shown in Fig. 3c, d. Based on the surface potential morphology of the cross section, distinct regions corresponding to Al layer, Al—Si alloy layer (the dark red area between Al and Si), and the silicon region containing BSF can be clearly identified. Fig. 3e, f present the surface potential curves across these layers. The surface potential constantly increases from the bulk phase of Si to the

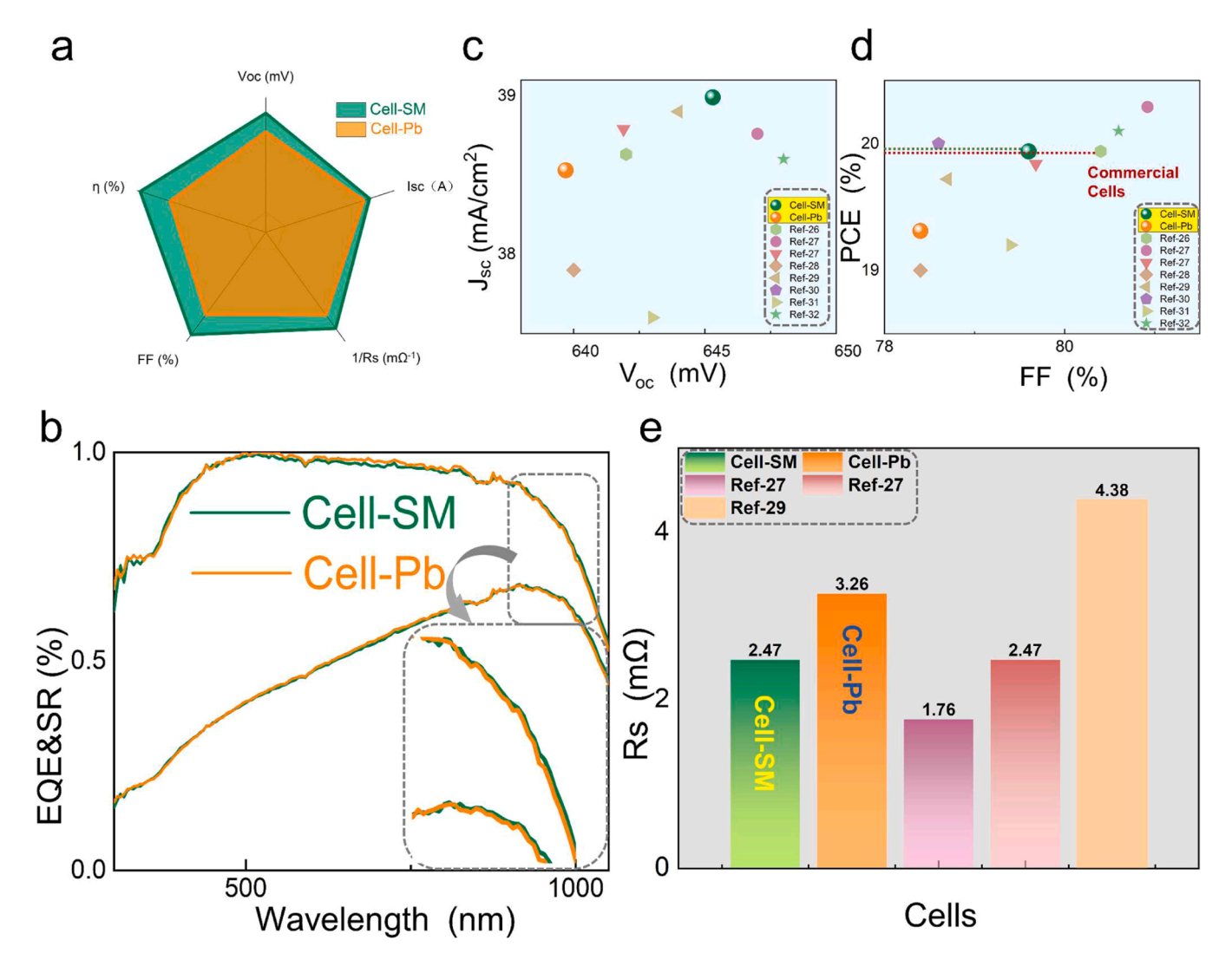


Fig. 2. Photovoltaic characteristics of cells. (a) Performance radar chart of the Cell-SM and the Cell-Pb; (b) External quantum efficiency (EQE) measurements and spectral response (SR) curves of the Cell-SM and the Cell-Pb; (c-e) Comparison between the photovoltaic characteristics of monocrystalline c-Si solar cells in other studies and the solar cell developed within this work; (c) J_{sc} and V_{oc} ; (d) PCE and FF; (e) R_s .

bulk phase of Al. The magnitude of the surface potential step between the bulk phases of Al and Si was found to be 518 and 396 mV for Cell-SM and Cell-Pb, respectively. This surface potential step is attributed to the built-in electric field and the gradient of hole density, which affect the redistribution of holes at the Al-Si interface and are correlated the quality of Al-Si interface [36-39]. A good contact with hole-selectivity results in improved carrier collection and higher hole density, leading to an increase in the magnitude of the whole potential skip-step [39]. The large surface potential step observed in Cell-SM confirms the improvement of Al-Si contact on the back surface, which likely contributes to the decrease in R_s and increase in I_{sc} . Additionally, the surface potential step in the Al-Si alloy layer is also noteworthy. The value of surface potential step in the Al-Si alloy layer of the Cell-SM is 73 mV with a change rate of 25.1 mV/µm, while the value for Cell-Pb is 25.6 mV with a change rate of 14.54 mV/µm. This indicates that the Al-Si interface of the Cell-SM is superior to that of Cell-Pb in terms of surface potential, further confirming the optimization of the Al-Si contact in Cell-SM.

To effect of SM-g on the back of cell and the Al-Si interface was investigated through various measurements. Scanning electron microscopy (SEM) images in Fig. 4b, d show the surface structure after sintering of Cell-SM and Cell-Pb, respectively. The spherical bright small particles are aluminium powder, while the dark holes are the shells left

by the melting of aluminium particles [9]. It is evident that there are more dark holes in Cell-SM than in Cell-Pb, indicates that SM-g greatly enhances the sintering effect [8]. This is supported by Fig. 1d, where P-SM provides heat from the thermite reaction to melt more aluminium particles and produce more dark holes in Cell-SM, which is beneficial to the sintering of aluminium paste (the SEM images with larger field of views were shown in Fig. S5, Supporting Information) [27]. Cross-sectional images of Cell-SM and Cell-Pb in Fig. 4c and d, respectively, show the BSF layers marked with green and yellow dashed lines. Upon comparison, it can be seen that the thickness of BSF layer in Cell-SM is $6.05 \mu m$, which is twice that of Cell-Pb (original images are shown in Fig. S6, Supporting Information). The BSF layer was formed by the diffusion of elements such as aluminum into the bulk phase of silicon during sintering. The SEM images combined with corresponding energy dispersive X-ray spectroscopy (EDS) mappings of the back of Cell-SM after removing the aluminum layer are shown in Fig. S7, Supporting Information. P-SM containing SM-g provided heat from the thermite reaction, which enhanced the diffusion process to form a thick BSF layer. The thickness of BSF layer was positively correlated with V_{oc} and minority carrier lifetime, which improved the efficiency of cell. The increase in the thickness of the BSF layer of Cell-SM explains the characteristics of a high V_{oc} . To further understand the diffusion process, a sample of the interface between the Al-Si alloy layer and the BSF layer

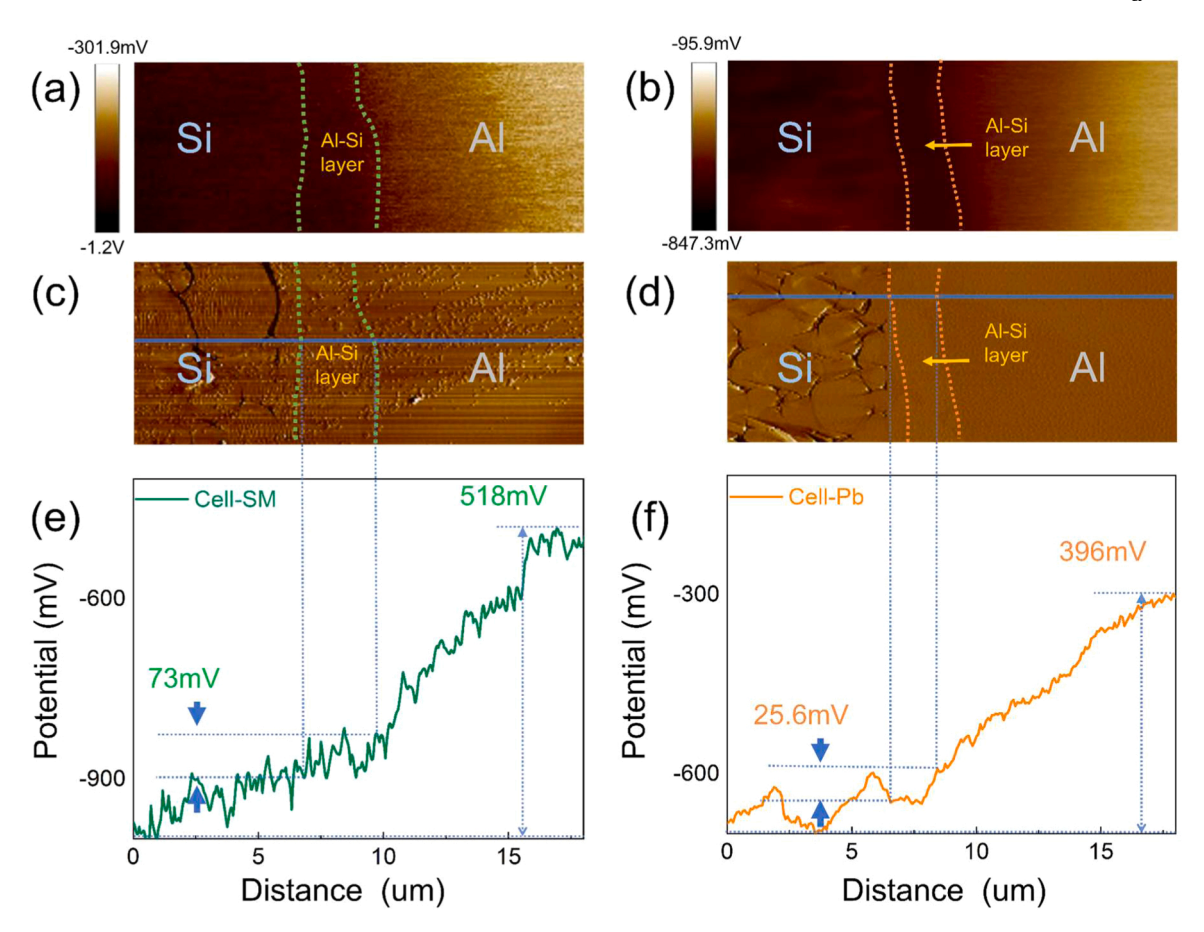


Fig. 3. Surface potential images, topography and surface potential line profiles of cells. (a-b) surface potential images of the Cell-SM and the Cell-Pb, respectively; (c-d) morphology images of the Cell-SM and Cell-Pb, respectively; (e-f) Surface potential curves of the Cell-SM and the Cell-Pb, respectively.

was extracted by focused ion beam (FIB) and measured by transmission electron microscopy (TEM) and EDS. The morphology and elemental distribution at the interface between the Al-Si alloy layer and the BSF layer are shown in Fig. 4f-k. From the top left corner to the bottom right corner, Si in cyan gradually deepens while Al in green, Sb in purple, and Mo in yellow gradually become shallower. The depth of color represents the degree of enrichment of the element, indicating that these elements diffuse with each other during sintering. Although O in red is concentrated in the upper left corner area surrounded by the dotted line, there is still a small amount of O in the internal area, possibly due to the formation of oxides on the side near the Al-Si alloy. (TEM images of a larger area combined with corresponding the EDS mappings of the interface extracted by FIB between Al and Si of Cell-SM are shown in Fig. S8, Supporting Information.) In order to further study the diffusion of elements, the content of Al, Mo and Sb at different depths was analyzed by EDS point scan mode and the result is shown in Fig. 4l. As the points continue to approach the interior zone, the ratio of Al to Mo and Sb increases from 2.87 to 3.50, and the ratio of Mo to Sb increases from 3.03 to 5.00 (raw data is shown in Fig. S9, Supporting Information). The gradient distribution of Mo may increase V_{oc} by changing the surface band bending at the junction p-c-Si/Al and reduce Al-Si contact resistance by work function matching.

To determine the valence states of elements at the Al-Si interface of Cell-SM, X-ray photoelectron spectroscopy (XPS) measurements were performed and the results are shown in Fig. 5. Fig. 5a-d show the XPS spectra of Mo $3d_{5/2}$ with different etching times of 0, 20, 40 and 60 s, corresponding to etching depths approximately 0, 10, 20, and 30 nm. The 3d5/2 peak of Mo on the surface of the Al-Si interface is centered at 232.83 eV, and the 3d3/2 peak is centered at 235.98 eV, both matching the characteristic peaks of MoO_3 [40,41]. As the etching depth

increases, the 3d5/2 peak shifts to 228.3 eV and the 3d3/2 peak shifts to 231.5 eV, which correspond to the characteristic peaks of Mo⁰ (the XPS spectrum of Mo for Cell-SM without baseline and fitting curves shown in Fig. S10) [42]. This indicates the presence of molybdenum trioxide in the oxide layer on the surface layer, while metallic Mo was present in the internal area. Metallic Mo has a high work function in p-type Si, resulting in a lower barrier, which is beneficial for hole transport through the potential barrier, thereby reducing the contact resistance between Al and Si. The XPS spectra and fitting results of Sb 3d_{5/2} with different etching depths are shown in the Fig. 5e-h. The center position of the 3d5/2 peaks at different etching times is around 532.4 \pm 0.2 eV, matching the characteristic peaks of Sb₂O₅ [43,44]. Additionally, the peaks of deeper etching show a slight shift about of 0.3 eV. In contrast, the XPS spectra and fitting results of Sb 3d_{5/2} in SM-g and cell doped with only Sb are around 530.5 \pm 0.2 eV, corresponding to Sb₂O₃ (shown in Fig. S11b and g-j, Supporting Information) [45]. The formation of Sb₂O₅ is conducive to achieving low sheet resistance and shallow doping [46]. Meanwhile, Fig. 5i-l show the XPS spectra and fitting results of Al. The 2p peak of Al with 0 s etching is centered at 74.8 eV, matching the characteristic peaks of Al₂O₃/Al [47,48]. Compared to the peak of Al with 0 s etching, the peaks of Al with 20 s, 40 s, and 60 s etching show an obvious shift of about 1 eV. This is attributed to the oxidation reaction of aluminum in the lower area, causing these peaks to shift from 74.8 eV to 75.9 eV [48,49]. For further comparison, Cell-Pb was also measured under the same conditions, and the peak position of Al 2p does not shift at different etching times, indicating no additional oxidation reaction (shown in Fig. S11c-f, Supporting Information).

By combining the results of DTA in Fig. 1e and XPS in Fig. 5, it can be determined that a thermite reaction occurs during the sintering process. Under this condition, MoO₃, which is a strong oxidizing agent, can

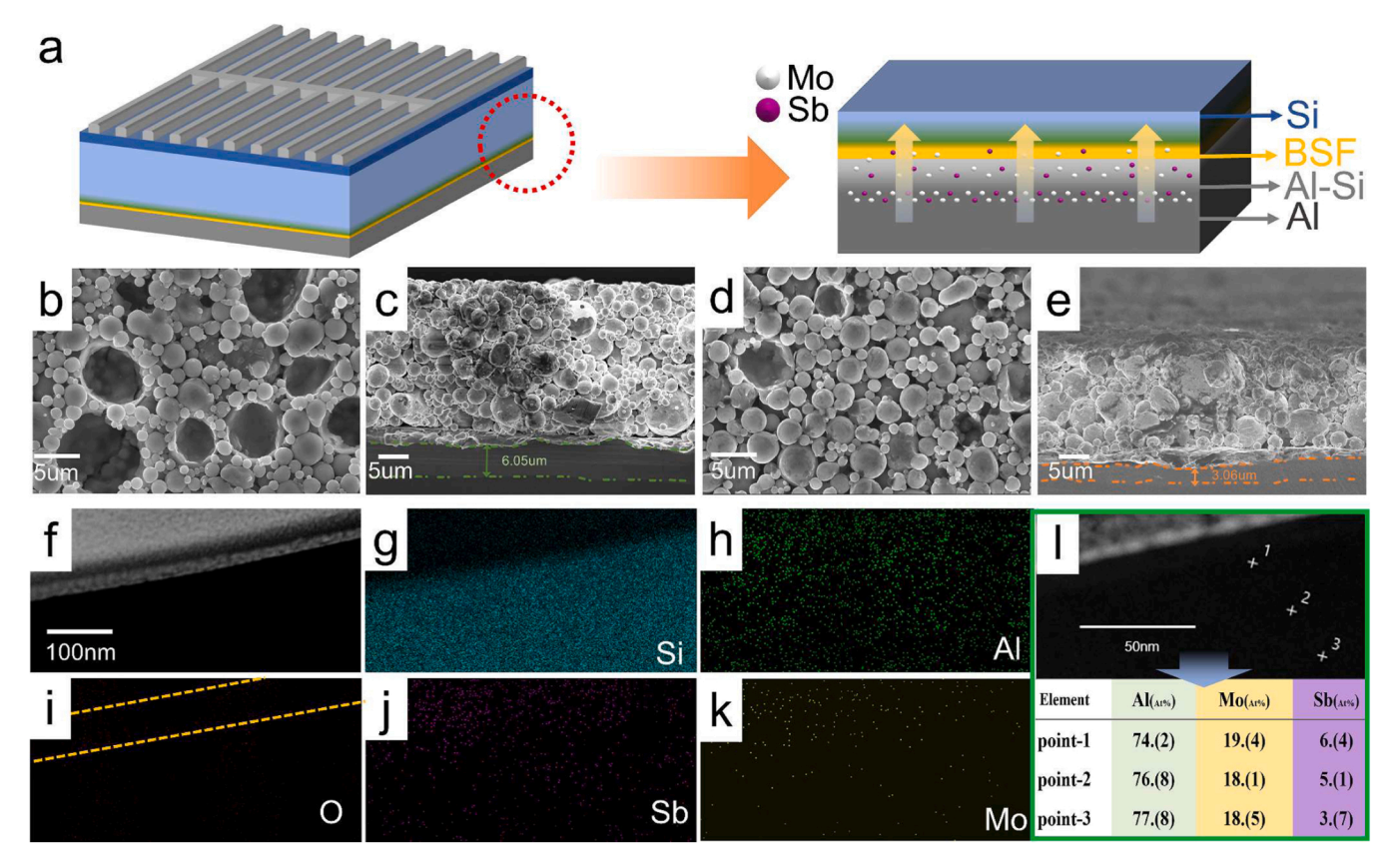


Fig. 4. Surface and cross-sectional morphology images by SEM, Al-Si interface images by TEM and elements distribution at the interface by EDS. (a) the Schematic diagram of the Al-Si interface; (b) the Al layer surface on the back of the Cell-SM; (c) the Cross section of the Cell-SM; (d) Al layer surface on the back of the Cell-Pb; (e) the Cross section of the Cell-Pb; (f-k) the Morphology and elements distribution at the interface between Al-Si alloy layer and BSF layer for Cell-SM; (l) Elements proportion of point-1, 2 and 3.

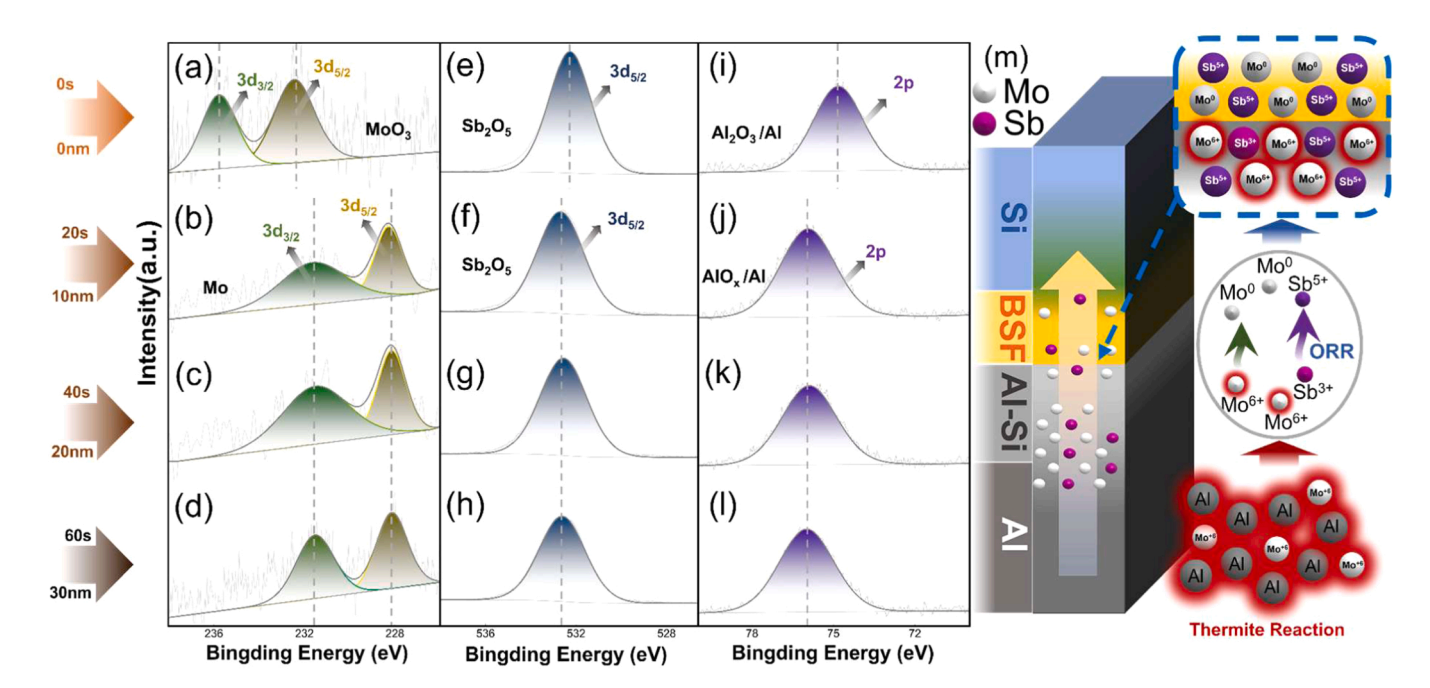


Fig. 5. XPS spectra and fitting results of the Al–Si solid layer of the Cell-SM etched 0, 20, 40 and 60 s with Ar+ sputtering. (a-d) XPS Mo $3d_{3/2}$ and $3d_{5/2}$ spectra and fitting results of the Cell-SM; (e-h) XPS Al 2p spectra and fitting results of the Cell-SM; (m) Schematic diagram of elements diffusion and ORR.

oxidize other elements, leading to an increase in the binding energy of these elements. The results of TEM and EDS in Fig. 4 and XPS in Fig. 5 show that MoO₃, Sb₂O₅, Al2O3 and Al exist on the surface of the Al-Si alloy layer. Meanwhile, Mo⁰ exists in deeper positions along with high valence Al and Sb. These results confirm the oxidation of Al and Sb, and the reduction of Mo. Fig. 5m illustrates the process of element diffusion and the oxidation-reduction reactions (ORR) caused by the thermite reaction, as well as the distribution of elements with different valence states at the Al-Si interface. The cells in this work were made of the same commercial front silver paste, and it was found that changes in resistance, other than Al-Si contact resistance, had little impact (as shown in Fig. S12). Combining the XPS and KPFM results, it can be concluded that the Sb/Mo co-doped Al-Si interface structure, constructed by the redox reactions induced by the thermite reaction, improves hole selectivity and optimizes the Al-Si contact, resulting in a decrease in R_s and an increase in FF and PCE. In comparison, the effects of Sb-doping (marked as B-Sb) and Mo-doping (marked as B-Mo) alone are less pronounced (listed in Table S3, Supporting Information). The Al layer of the cell made by B-Sb has almost no dark holes, and the BSF layer is relatively thin, indicating poor sintering. The results of element distribution show that Sb is close to the Al-Si alloy layer. The XPS spectra and fitting results of B-Sb are corresponding to Sb₂O₃, and the valence state of Al did not change at different etching times, which implies no redox reaction occurred (shown in Fig. S13). The solar cell manufactured by B-Sb obtained a V_{oc} of 636.4 mV, a I_{sc} of 8.943 A, and a R_s of 5.108 m Ω . This leads to a high PCE of 18.11% (in Table S3). The Al layer of the cell made by B-Mo has some dark holes, and the BSF layer is thicker than B-Sb but thinner than Cell-SM, which means that the sintering of B-Mo is better than that of B-Sb but inferior to Cell-SM. The results of element distribution show that Mo is close to the Al-Si alloy layer. The XPS spectrum and fitting results show that the valence state of Mo and Al have changed at different etching times, which indicates redox reaction occurred (shown in Fig. S14). The solar cell manufactured by B-Mo obtained a V_{oc} of 633.3 mV, a I_{sc} of 9.071 A, and a R_s of 3.477 m Ω . This leads to a high PCE of 18.47%(in Table S3). Therefore, the co-effect of Sb and Mo can obtain the performance of Cell-SM.

In the future directions of our research, it is attemptable that change the relevant properties of glass frits by adjusting the proportion of the main oxides. We have tried using some glass frits with different oxides ratios to make cells, but have not been able to further improve efficiency (Table S4). Adjustment of proportion requires more experiments to explore. It is also worth studying to further reduce the glass transition temperature by adding new low melting point oxides. In addition, adding a small amount of alkali metal oxides is also a feasible strategy, which is widely applied in the manufacturing of other type of glass frits.

4. Conclusions

In conclusion, a new glass frits with a low T_g was designed and added into Al paste to achieve a good Al-Si contact and a thick BSF layer through a thermite reaction during the sintering process, resulting in enhanced performance of monocrystalline c-Si solar cells. At the inner region of the Al-Si interface, MoO₃ with strong oxidizing properties was reduced to metallic Mo, while Sb₂O₃ was oxidized to Sb₂O₅, and Al was oxidized to Al₂O₃. The Sb/Mo co-doped Al-Si interface constructed by the thermite reaction reduced the contact barrier between aluminum and silicon, and minimized carrier recombination, facilitating the transport of holes to the Al layer for collection. As a result, the solar cell manufactured with this glass frits exhibited a high V_{oc} , a high I_{sc} , and a lower R_s . This leads to a high PCE of 19.93%, which is comparable to commercial products. This finding provides a new approach for regulating elements and their valence states at the interface. The B2O3- Sb_2O_3 -MoO₃ glass frits, as a new type of low T_g glass frits, shows great potential for application in electronic paste and deserves further research. This approach can be extended to other devices that required better Al-Si contact, such as metallization of the back of p-Si solar cells,

the front of n-Si solar cells, and silicon-based devices, which are currently attracting extensive attention.

Supplementary materials

SEM images combined with corresponding the EDS mappings of the SM-g and SEM images of the Pb-g; IV curves of the Cell-SM and the Cell-Pb; SEM images of cross section area of the Cell-SM and the Cell-Pb; SEM images combined with corresponding the EDS mappings of the back of the Cell-SM after removing the aluminum layer; TEM large scale images combined with corresponding the EDS mappings of the interface extracted by FIB between Al and Si of the Cell-SM; TEM images combined with corresponding EDS spectra of point-1, 2 and 3 at the interface between Al and Si; XPS spectra and fitting results of the SM-g and the Cell-Pb and Cell without Mo; Contact resistance between Ag and Si and sheet resistance of the Al conducting film of the Cell-SM and the Cell-Pb; Photovoltaic performance parameters of Cells manufactured with different amounts of the SM-g added; Photovoltaic performance parameters of Cells manufactured with the SM-g, B₂O₃-MoO₃ glass frits and B₂O₃-Sb₂O₃ glass frits.

CRediT authorship contribution statement

Yongsheng Li: Conceptualization, Methodology, Investigation, Writing – original draft. Ziwei Chen: Investigation, Writing – review & editing. Bo Zhang: Investigation. Haibiao Chen: Writing – review & editing. Rui Zhou: Resources. Boweng Nan: Resources. Wenguang Zhao: Resources. Ke Li: Resources. Bolin Zhao: Resources. YinGuo Xiao: Resources. Jian Liu: Resources. Jun Chen: Writing – review & editing, Resources. Yuan Lin: Writing – review & editing, Project administration, Feng Pan: Funding acquisition, Project administration, Writing – review & editing.

Declaration of Competing Interest

The authors declare that they have no known competing financial interests or personal relationships that could have appeared to influence the work reported in this paper.

Data Availability

Data will be made available on request.

Acknowledgments

The author would thank the support of the Soft Science Research Project of Guangdong Province (No. 2017B030301013), and Guangdong Innovative Team Program (No. 2013N080).

Appendix A. Supporting information

Supplementary data associated with this article can be found in the online version at doi:10.1016/j.nanoen.2023.108801.

References

- S. Chu, A. Majumdar, Opportunities and challenges for a sustainable energy future, Nature 488 (2012) 294–303.
- [2] J.P. Helveston, G. He, M.R. Davidson, Quantifying the cost savings of global solar photovoltaic supply chains, Nature 612 (2022) 83–87.
- [3] H. Liang, F. You, Reshoring silicon photovoltaics manufacturing contributes to decarbonization and climate change mitigation, Nat. Commun. 14 (2023) 1274.
- [4] T. Kirchartz, U. Rau, What makes a good solar cell? Adv. Energy Mater. 8 (2018).
- [5] A.G. Aberle, Surface passivation of crystalline silicon solar cells: a review, Prog. Photo Res Appl. 8 (2000) 473–487.
- [6] Soon-gil K., In-jae L., Sang-gon K., et al. Enhancing the solar cell efficiency with optimized metal paste. 10th IEEE International Conference on Nanotechnology and Joint Symposium with Nano Korea 2010 KINTEX (IEEE-NANO 2010), 2010, 1151–1155.

- [7] H. Wang, S. Ma, M. Zhang, et al., Effects of screen printing and sintering processing of front side silver grid line on the electrical performances of multi-crystalline silicon solar cells, J. Mater. Sci: Mater. Electron 28 (2017) 11934–11949.
- [8] J.H. Yi, H.Y. Koo, J.H. Kim, et al., Fine size pb-based glass frit with spherical shape as the inorganic binder of al electrode for si solar cells, J. Alloy. Compd. 490 (2010) 488–492.
- [9] B.-N. Kim, D.-H. Kim, H.-J. Kim, et al., Characterization and cell performance of al paste with an inorganic binder of bi2o3–b2o3–zno system in si solar cells, Curr. Nanosci. 10 (2014) 66–69.
- [10] R.A. Smith, Boron in glass and glass making, J. Non-Cryst. Solids 84 (1986) 421–432.
- [11] J.A. Amick, F.J. Bottari, J.I. Hanoka, The effect of aluminum thickness on solar-cell performance, J. Electrochem. Soc. 141 (1994) 1577–1585.
- [12] G. Du, B. Chen, N. Chen, et al., Efficient boron doping in the back surface field of crystalline silicon solar cells via alloyed-aluminum-boron paste, IEEE Electron Device Lett. 33 (2012) 573–575.
- [13] D. Scirè, P. Procel, A. Gulino, et al., Sub-gap defect density characterization of molybdenum oxide: an annealing study for solar cell applications, Nano Res. 13 (2020) 3416–3424.
- [14] X. Zhang, G. Wu, Z. Gu, et al., Active-layer evolution and efficiency improvement of (ch3nh3 3bi2i9-based solar cell on tio2-deposited ito substrate, Nano Res. 9 (2016) 2921–2930.
- [15] C. Mader, J. Müller, S. Eidelloth, et al., Local rear contacts to silicon solar cells by in-line high-rate evaporation of aluminum, Sol. Energy Mater. Sol. Cells 107 (2012) 272–282.
- [16] M. Bivour, J. Temmler, H. Steinkemper, et al., Molybdenum and tungsten oxide: High work function wide band gap contact materials for hole selective contacts of silicon solar cells, Sol. Energy Mater. Sol. Cells 142 (2015) 34–41.
- [17] J. Bullock, A. Cuevas, T. Allen, et al., Molybdenum oxide moox: a versatile hole contact for silicon solar cells, Appl. Phys. Lett. 105 (2014).
- [18] K.V D, K.E. Abraham, Multifunctional transition metal doped sb2o3 thin film with high near-ir transmittance, anti-reflectance and uv blocking features, Appl. Surf. Sci. 493 (2019) 1115–1124.
- [19] S.R. Wenham, J. Zhao, X. Dai, et al., Surface passivation in high efficiency silicon solar cells, Sol. Energy Mater. Sol. Cells 65 (2001) 377–384.
- [20] W.M. Werner, Work function difference of mos-system with aluminum field plates and polycrystalline silicon field plates, Solid-State Electron 17 (1974) 769–775.
- [21] B. Zhang, Y. Li, Y. Chen, et al., Interface tuning through the moo3 additive in al paste to enhance the performance of crystalline silicon solar cells, ACS Appl. Energy Mater. 5 (2022) 13254–13260.
- [22] H. Doweidar, K. El-Egili, R. Ramadan, et al., Structural investigation and properties of sb 2 o 3 –pbo–b 2 o 3 glasses, J. Non-Cryst. Solids 497 (2018) 93–101.
- [23] A. Tozri, M. Al-Zaibani, A. Shahboub, et al., Structure and related physical properties of li2o-sb2o3-b2o3 glasses, Phys. Scr. 97 (2022).
- [24] R.S. Iordanova, A.D. Bachvarova-Nedelcheva, L.I. Aleksandrov, et al., Synthesis of bibo3 by crystallization of glasses in the bi2o3-moo3-b2o3 system, Bulg. Chem. Commun. 43 (2011) 254–258.
- [25] H.R. Yeom, S. Song, S.Y. Park, et al., Aesthetic and colorful: dichroic polymer solar cells using high-performance fabry-pérot etalon electrodes with a unique sb2o3 cavity, Nano Energy 77 (2020).
- [26] L.G. Gerling, C. Voz, R. Alcubilla, et al., Origin of passivation in hole-selective transition metal oxides for crystalline silicon heterojunction solar cells, J. Mater. Res. 32 (2016) 260–268
- [27] Y.J. Fan, P.D. Han, P. Liang, et al., Investigation of the forming process and characteristics of al-bsf in silicon solar cells, in: Proceedings of the International Conference on Materials for Renewable Energy and Environment (ICMREE), Chengdou, PEOPLES R CHINA, 2013, Ieee, NEW YORK, , 2014.
- [28] N. Chen, A. Ebong, Towards 20% efficient industrial al-bsf silicon solar cell with multiple busbars and fine gridlines, Sol. Energy Mater. Sol. Cells 146 (2016) 107-113
- [29] K.H. Kim, C.S. Park, J.D. Lee, et al., Record high efficiency of screen-printed silicon aluminum back surface field solar cell: 20.29%, Jpn. J. Appl. Phys. 56 (2017).
- [30] M.Z. Rahman, Status of selective emitters for p-type c-si solar cells, Opt. Photonics J. 02 (2012) 129–134.
- [31] M.A. Awaah, I. Awaah, V.A. Apalangya, et al., Investigation and characterization of al paste as back surface field (bsf) for high efficiency si solar cell, 2021 IEEE PES/ IAS Power (2021) 624–628.
- [32] A. Das, V. Meemongkolkiat, D. Kim, et al., 20% efficient screen-printed cells with spin-on-dielectric-passivated boron back-surface field, IEEE Trans. Electron Devices 57 (2010) 2462–2469.
- [33] E. Cho, A. Rohatgi, Y.-W. Ok, Comparison of light-induced degradation and regeneration in p-type monocrystalline full aluminum back surface field and passivated emitter rear cells, Curr. Appl. Phys. 18 (2018) 1600–1604.
- [34] T. Fellmeth, S. Mack, J. Bartsch, et al., 20.1% efficient silicon solar cell with aluminum back surface field, IEEE Electron Device Lett. 32 (2011) 1101–1103.
- [35] L. Wan, C. Zhang, K. Ge, et al., Conductive hole-selective passivating contacts for crystalline silicon solar cells, Adv. Energy Mater. 10 (2020).
- [36] D.K. Schroder, D.L. Meier, Solar-cell contact resistance a review, IEEE Trans. Electron Devices 31 (1984) 637–647.
- [37] D. Pysch, A. Mette, S.W. Glunz, A review and comparison of different methods to determine the series resistance of solar cells, Sol. Energy Mater. Sol. Cells 91 (2007) 1698–1706.
- [38] H.H. Berger, Contact resistance and contact resistivity, J. Electrochem. Soc. 119 (1972) 507. -&.

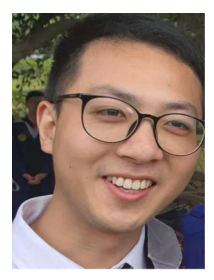
- [39] Y.-J. Chen, M.-J. Zhang, S. Yuan, et al., Insight into interfaces and junction of polycrystalline silicon solar cells by kelvin probe force microscopy, Nano Energy 36 (2017) 303–312.
- [40] M.A. Bica de Moraes, B.C. Trasferetti, F.P. Rouxinol, et al., Molybdenum oxide thin films obtained by the hot-filament metal oxide deposition technique, Chem. Mater. 16 (2003) 513–520.
- [41] H. Li, J. Chen, M. Cui, et al., Spray coated ultrathin films from aqueous tungsten molybdenum oxide nanoparticle ink for high contrast electrochromic applications, J. Mater. Chem. C. 4 (2016) 33–38.
- [42] Z. Song, T. Cai, Z. Chang, et al., Molecular level study of the formation and the spread of moo3 on au(111) by scanning tunneling microscopy and x-ray photoelectron spectroscopy, J. Am. Chem. Soc. 125 (2003) 8059–8066.
- [43] F. Montilla, E. Morallon, A. De Battisti, et al., Preparation and characterization of antimony-doped tin dioxide electrodes. Part 2. Xrd and exafs characterization, J. Phys. Chem. B 108 (2004) 5044–5050.
- [44] M. Sun, D.Z. Li, Y.B. Chen, et al., Synthesis and photocatalytic activity of calcium antimony oxide hydroxide for the degradation of dyes in water, J. Phys. Chem. C. 113 (2009) 13825–13831.
- [45] M. Oku, S. Suzuki, H. Kimura, et al., Oxidation behavior of antimony segregated surfaces of iron antimony alloy investigated by xps, Appl. Surf. Sci. 20 (1985) 549–563.
- [46] B. Kalkofen, A.A. Amusan, M. Lisker, et al., Application of atomic layer deposited dopant sources for ultra-shallow doping of silicon, Phys. Status Solidi C. 11 (2013) 41–45.
- [47] T. Tago, N. Kataoka, H. Tanaka, et al., Xps study from a clean surface of al2o3 single crystals, Jun 18-23, in: Proceedings of the 9th International Conference on Materials for Advanced Technologies (ICMAT) / Symposium on Stimuli-Sensitive and-Responsive Polymer Biomaterials, Singapore, SINGAPORE, 2017, Elsevier Science By, AMSTERDAM, 2017.
- [48] S.L. Chang, J.W. Anderegg, P.A. Thiel, Surface oxidation of an al-pd-mn quasicrystal, characterized by x-ray photoelectron spectroscopy, J. Non-Cryst. Solids 195 (1996) 95–101.
- [49] Y.L. Yan, M.A. Helfand, C.R. Clayton, Evaluation of the effect of surface-roughness on thin-film thickness measurements using variable angle xps, Appl. Surf. Sci. 37 (1989) 395–405.



Yongsheng Li received his bachelor's degree of engineering from the School of Metallurgy and Environment at Central South University in 2018. He is currently is pursuing his Ph. D. degree in the School of Advanced Materials, Peking University under the supervision of Prof. Feng Pan. His research interest is the synthesis of metalized materials for solar cells.



Ziwei Chen received his bachelor's degree of engineering from the School of Material Science and Chemical engineering at Ningbo University in 2019. He is currently is pursuing his Ph. D. degree in the School of Advanced Materials, Peking University under the supervision of Prof. Yinguo Xiao. His research interest is the synthesis of layered cathode materials and structure characterization based on X-ray and neutron diffraction methods.



Bo Zhang received his bachelor's degree of engineering from Nanchang University in 2019 and master of science degree from the School of Advanced Materials, Peking University in 2022.



Haibiao Chen Ph.D. in Materials Science and Engineering, Associate Researcher, Master's Supervisor at Shenzhen Vocational and Technical College. His main research directions are porous materials, organic precursor conversion ceramics, composite materials, and catalysts.



Bolin Zhao Analysis and testing Engineer, Materials Testing Center, School of New Materials, Shenzhen Graduate School, Peking University.



Rui Zhou received his bachelor's degree of engineering from Harbin Institute of Technology. He is currently is pursuing his Ph. D. degree in the School of Advanced Materials, Peking University under the supervision of Prof. Feng Pan. His research interest is solar cells.



Prof. Yinguo Xiao received his Ph.D. degree from Institute of Physics, Chinese Academy of Sciences, China in 2006. He was a postdoctoral fellow from 2007 to 2009 and a research scientist from 2009 to 2014 at Juelich Research Centre (Forschungszentrum Jülich), Germany. He became a tenured staff scientist in Juelich Research Centre since 2015. In 2017, he joined Peking University Shenzhen Graduate School, China as an associate professor. His research interests are on research and development of energy *materials*, magnetic materials, *and characterization of* complex materials using X-ray and neutron scattering techniques.



Bowen Nan Analysis and testing Engineer, Materials Testing Center, School of New Materials, Shenzhen Graduate School, Peking University.



Jian Liu He is currently is pursuing his Ph. D. degree in the School of Advanced Materials, Peking University under the supervision of Prof. Feng Pan. His research interest is silver paste for solar cells.



Wenguang Zhao is pursuing his Ph. D. degree in the School of Advanced Materials, Peking University. He has over 10 years' experience in material characterization using wide range of analytical tools including XRD, XPS, SEM and TEM. His research interests mainly focus on the Ex/in-situ TEM and Ex/in-situ XRD characterization of battery materials.



Jun Chen received his Ph.D. degree in 2021 at Beijing Normal University, China. Currently, he is working as a full faculty member at Institute of Zhejiang University-Quzhou. His research focuses on electrodes (modified by ion beam technology), binders, and electrolytes for energy storage applications including lithium-ion batteries, sodium ion batteries, and lithium-metal batteries.



Ke Li Analysis and testing Engineer, Materials Testing Center, School of New Materials, Shenzhen Graduate School, Peking University.



Prof. Yuan Lin Institute of Chemistry, Chinese Academy of Sciences (CAS), got B.S. from Dept. Chemistry, Peking University in1985, M.S and PhD from CAS in 1988 and 1995, respectively. In 1988–1999, he took the position of assistant professor at Institute of Photographic Chemistry, Chinese Academy of Sciences. From 1999 to present, he took the position of full professor. For more than 20 years, Prof. Lin has been engaged in the fields of photoelectrochemical conversion of solar energy, preparation of nanocrystalline semiconductors, investigation of photoelectrochemical and surface properties of nanocrystalline semiconductors, developing ionic liquid and polymeric materials for electrolytes.



Prof. Feng Pan National 1000-plan Professor, Founding Dean of School of Advanced Materials, Peking University Shenzhen Graduate School, Director of National Center of Electric Vehicle Power Battery and Materials for International Research, got B.S. from Dept. Chemistry, Peking University in1985 and PhD from Dept. of P & A Chemistry, University of Strathclyde, Glasgow, UK, with "Patrick D. Ritchie Prize" for the best Ph.D. in 1994. With more than a decade experience in large international incorporations, Prof. Pan has been engaged in fundamental research and product development of novel optoelectronic and energy storage materials and devices. As Chief Scientist, Prof. Pan led 8 entities in Shenzhen to win the 150 million RMB grant for the national new energy vehicles

(power battery) innovation project since 2013. As Chief Scientist, Prof. Pan led 12 entities to win National Key project of Material Genomic Engineering for Solid State Li-ion Battery in China in 2016.